

Spin Hall effect in spin-valley coupled monolayer transition-metal dichalcogenides

Wen-Yu Shan,¹ Hai-Zhou Lu,² and Di Xiao¹

¹*Department of Physics, Carnegie Mellon University, Pittsburgh, Pennsylvania 15213, USA*

²*Department of Physics, The University of Hong Kong, Pokfulam Road, Hong Kong, China*

We study both the intrinsic and extrinsic spin Hall effect in spin-valley coupled monolayers of transition metal dichalcogenides. We find that whereas the skew-scattering contribution is suppressed by the large band gap, the side-jump contribution is comparable to the intrinsic one with opposite sign in the presence of scalar and magnetic scattering. Intervalley scattering tends to suppress the side-jump contribution due to the loss of coherence. By tuning the ratio of intra- to intervalley scattering, the spin Hall conductivity shows a sign change in hole-doped samples. Multiband effect in other doping regime is considered, and it is found that the sign change exists in the heavily hole-doped regime, but not in the electron-doped regime.

PACS numbers: 72.10.-d, 72.25.Dc, 73.63.-b, 75.70.Tj

I. INTRODUCTION

Monolayers of transition-metal dichalcogenides MX_2 ($M = \text{Mo}, \text{W}, X = \text{S}, \text{Se}$) have attracted intense recent interest due to their unique optical and electronic properties.¹ These two-dimensional materials can be regarded as semiconductor analog of graphene: their band structure consists of two degenerate but inequivalent valleys located at the corners of the hexagonal Brillouin zone, with a direct band gap in the visible frequency range.^{2,3} It was predicted that,^{4,5} due to the lack of inversion center in the crystal structure, the two valleys can be distinguished by the Berry phase of the Bloch bands,⁶ which gives rise to the valley Hall effect and valley-dependent optical selection rule.^{7,8} This prediction has motivated several recent experiments, in which the optical generation^{5,9,10} and electric control¹¹ of valley polarization have been demonstrated.

Another interesting property of MX_2 is the large spin-orbit coupling (SOC) derived from the heavy metal d -orbitals.¹² It was pointed out that broken inversion symmetry also gives rise to a strong spin-valley coupling,⁴ i.e., carriers in opposite valleys have opposite spin moment (Fig. 1). This coupling has a number of implications. First, various valley-dependent phenomena now become spin-dependent. In particular, the valley Hall effect is accompanied by a spin Hall effect, in which a transverse spin current can be generated by a longitudinal electric field. Secondly, the spin-valley coupling dictates that intravalley scattering conserves the spin index whereas intervalley scattering necessarily flips it, resulting in prolonged spin lifetime in the diffusion regime.¹³ The intra- and inter-valley scattering also leads to opposite localization behavior.¹⁴

In general, the spin Hall effect consists of both intrinsic and extrinsic contributions. The intrinsic part, determined by the Berry curvature of the Bloch bands,^{15,16} has been discussed for monolayer MX_2 in the clean limit, based on first-principles band-structure calculations.¹⁷ On the other hand, it is well known that impurity scattering could modify the intrinsic contribution as demon-

strated in the Rashba model.^{18–20} Furthermore, impurity scattering itself may lead to extrinsic spin Hall effect,^{21–23} including both skew-scattering²⁴ and side-jump²⁵ mechanisms. Since the strong spin-valley coupling severely limits the possible scattering channels, it is important to investigate its role in the spin Hall effect in MX_2 monolayers.

In this work, we calculate the spin Hall conductivity (SHC) of MX_2 monolayers. We find that symmetric vertex correction has little effect on the intrinsic contribution due to the large band gap. For the extrinsic mechanisms, the side-jump contribution is comparable to the intrinsic contribution, while the skew scattering contribution is suppressed by the large band gap for both scalar and magnetic scattering. In hole-doped samples, the sign of the SHC is opposite for the side-jump and intrinsic contributions, and the side-jump contribution is always suppressed by intervalley scattering due to the loss of coherence. Hence, by tuning the relative strength of intra- and intervalley scattering, the total SHC shows a sign change, i.e., it is negative for weak intervalley scattering and positive for strong intervalley scattering. Our study is also extended to the multiband case when the system

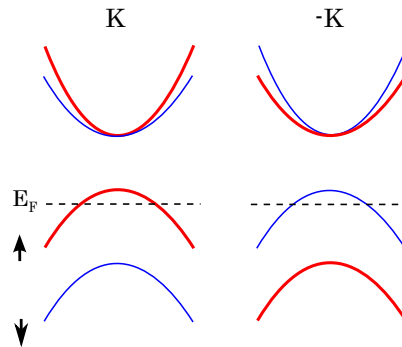


FIG. 1: (Color online) Schematics of low-energy band structure for monolayer MX_2 . Red (blue) curves represent bands with spin up (down). Black dashed line shows the Fermi energy E_F measured from the middle of the gap.

is electron- or heavily hole-doped. We find that the sign change exists in the hole-doped regime, but not in the electron-doped regime. Therefore, the SHC may provide another measure to determine the strength of intervalley scattering in hole-doped MX_2 monolayers.

This paper is organized as follows. In Sec. II we describe the effective model of monolayer MX_2 at valley $\pm K$. In Sec. III we introduce some important definitions, including scattering potential, relaxation time and vertex correction. The result of the SHC is presented in Sec. IV and V for lightly hole-doped case and the multi-band case (electron- or heavily hole-doped regime), respectively. Finally, a discussion and conclusion is given in Sec. VI.

II. MODEL

Monolayers of MX_2 has the crystal symmetry D_{3h} . The electronic properties due to inversion symmetry breaking and large atomic SOC from metal d orbitals are captured by the low-energy effective model around the zone corners $K(-K)$.⁴

$$H = at(\tau k_x \hat{\sigma}_x + k_y \hat{\sigma}_y) + \frac{\Delta}{2} \hat{\sigma}_z - \lambda \tau \hat{s}_z \otimes \frac{\hat{\sigma}_z - 1}{2}, \quad (1)$$

where $\hat{\sigma}$ and \hat{s} act on the orbital $\{d_{z^2}, (d_{x^2-y^2} + i\tau d_{xy})/\sqrt{2}\}$ and spin space, respectively. \otimes is the Kronecker product. $\tau = \pm 1$ refers to $\pm K$ valley. Δ is the energy gap, a is the lattice constant, t is the hopping integral, and λ is the spin-orbit coupling constant. Note that the complex orbital basis are orthogonal to each other, reducing the coherence of intervalley scattering.

The band dispersion reads

$$E_{\tau,s}^m = \tau s \frac{\lambda}{2} \pm m \sqrt{\left(\frac{\Delta}{2} - \tau s \frac{\lambda}{2}\right)^2 + a^2 t^2 k^2}, \quad (2)$$

where $m, \tau, s = \pm 1$ correspond to the conduction (valence) band, the valley K ($-K$) and the spin up (down) state, respectively. The dispersion is shown schematically in Fig. 1. For each band, eigenfunctions are given by

$$\begin{aligned} |c, \tau K, s\rangle &= |s\rangle \otimes \begin{pmatrix} \chi_n \\ \tau w_n e^{i\tau\varphi_{\mathbf{k}}} \end{pmatrix} \\ |v, \tau K, s\rangle &= |s\rangle \otimes \begin{pmatrix} w_n \\ -\tau \chi_n e^{i\tau\varphi_{\mathbf{k}}} \end{pmatrix} \end{aligned} \quad (3)$$

where c/v labels the conduction (valence) band. $n = 1, 2$ for $\tau s = \pm 1$, respectively, i.e., $n = 1$ for (K, \uparrow) and $(-K, \downarrow)$, and $n = 2$ for (K, \downarrow) and $(-K, \uparrow)$. χ_n, w_n are defined by

$$\chi_n = \cos \frac{\theta_n}{2}, \quad w_n = \sin \frac{\theta_n}{2}, \quad (4)$$

$$\cos \theta_n = \frac{\frac{\Delta}{2} + (-1)^n \frac{\lambda}{2}}{\sqrt{\left(\frac{\Delta}{2} + (-1)^n \frac{\lambda}{2}\right)^2 + a^2 t^2 k^2}}, \quad (5)$$

with $\tan \varphi_{\mathbf{k}} = k_y/k_x$.

III. DISORDER, RELAXATION TIME AND VERTEX CORRECTION

A. Impurity potentials

To calculate the extrinsic SHC, we apply the standard diagrammatic approach, in which the scattering due to impurities and disorders is treated as the perturbation to the eigenstates of H . We consider both scalar and magnetic impurities. Their potentials in real space can be modeled by

$$U(\mathbf{r}) = \sum_{i,\alpha=0,x,y,z} u_{\alpha}^i (\sigma_{\alpha} \otimes I) \delta(\mathbf{r} - \mathbf{R}_i), \quad (6)$$

where σ_{α} and I act on the spin and orbital space, respectively. \mathbf{R}_i and u represent the position and scattering strength of an impurity. We assume that the impurities have short-range potential and are delta-correlated, i.e., $\langle U(\mathbf{r}) \rangle_{dis} = 0$ and $\langle U(\mathbf{r})U(\mathbf{r}') \rangle_{dis} = nu^2 \delta(\mathbf{r} - \mathbf{r}')$, where n is the disorder concentration. Although intravalley scattering should be related to long-range potential, the practice by the delta potential is justified by numerical calculations.²⁶ In order to include the skew-scattering effect, third-order scattering correlation has to be considered $\langle U(\mathbf{r})U(\mathbf{r}')U(\mathbf{r}'') \rangle_{dis} = nv^3 \delta(\mathbf{r} - \mathbf{r}') \delta(\mathbf{r} - \mathbf{r}'')$.^{27,28}

With the potential and the eigenstates in Eq. (3), the scattering matrix elements for the intravalley scattering are found as

$$U_{\mathbf{k}\mathbf{k}'} = \sum_{i,\alpha=0,x,y,z} \frac{u_{\alpha}^i}{S} e^{i(\mathbf{k}' - \mathbf{k}) \cdot \mathbf{R}_i} (\sigma_{\alpha} \otimes I), \quad (7)$$

where S is the area of the system. Besides intravalley scattering, we also take into account intervalley scattering induced by short-range disorder.²⁹ The potential for the intervalley scattering is given by

$$\begin{aligned} U^I(\mathbf{r}) &= \sum_{i,\alpha=0,x,y,z} \sigma_{\alpha} \otimes \begin{pmatrix} t_{\alpha,A}^i \delta(\mathbf{r} - \mathbf{R}_i^A) & 0 \\ 0 & t_{\alpha,B}^i \delta(\mathbf{r} - \mathbf{R}_i^B) \end{pmatrix} \\ &\otimes \begin{pmatrix} 0 & e^{-i(\mathbf{K}' - \mathbf{K}) \cdot \mathbf{r}} \\ e^{i(\mathbf{K}' - \mathbf{K}) \cdot \mathbf{r}} & 0 \end{pmatrix}, \end{aligned} \quad (8)$$

where the basis of matrices represent spin, orbital and valley, respectively, and we have used A and B to label the two orbitals at each valley. For intervalley scattering, we also consider the scalar and magnetic impurities. Since B orbitals are orthogonal between different valleys, we can drop the corresponding part and obtain the scattering matrix element

$$U_{\mathbf{k},\mathbf{k}'}^I = \sum_i \begin{pmatrix} t_0^i + t_z^i & 0 & t_x^i - it_y^i & 0 \\ 0 & 0 & 0 & 0 \\ t_x^i + it_y^i & 0 & t_0^i - t_z^i & 0 \\ 0 & 0 & 0 & 0 \end{pmatrix} \frac{e^{i(\mathbf{k}' - \mathbf{k}) \cdot \mathbf{R}_i^A}}{S}. \quad (9)$$

With these scattering matrix elements, the correlation between them can be derived.

B. Relaxation times

The scattering will reduce lifetime of the eigenstates of H to finite. The lifetime can be defined with the help of relaxation times. Under the first-order Born approximation, the total relaxation time reads

$$\frac{1}{\tau} = \frac{1}{\tau_{intra}} + \frac{1}{\tau_{inter}}, \quad (10)$$

with the intravalley τ_{intra} and intervalley τ_{inter} defined as

$$\frac{1}{\tau_{intra}} = \frac{2\pi}{\hbar} N_1 (n_0 u_0^2 + n_z u_z^2) (w_1^4 + \chi_1^4), \quad (11)$$

$$\frac{1}{\tau_{inter}} = \frac{2\pi}{\hbar} N_1 (n_x t_x^2 + n_y t_y^2) w_1^4, \quad (12)$$

where $N_n = |\lambda/2 + (-1)^n E_F|/2\pi a^2 t^2$ is the density of states at the Fermi energy E_F . We introduce $N_{n=1,2}$ to describe the multiband effect. Note that $n = 1$ when $\tau s = 1$, which is for the highest two valence bands (K, \uparrow) and ($-K, \downarrow$).

We further introduce a set of effective relaxation times $\tau_{(n,p,q)}$ to include the multiband effect. We present the descriptions of the relaxation times in Table I, and the exact expressions in Appendix A. It is convenient to use these effective relaxation times to define the relaxation times of physical meanings. For example,

$$\frac{1}{\tau_{intra}} = \frac{w_1^4 + \chi_1^4}{\tau_{(1,1,1)}}, \quad \frac{1}{\tau_{inter}} = \frac{w_1^4}{\tau_{(1,2,2)}}. \quad (13)$$

Later we will see that $\tau_{(1,1,1)}/\tau_{(1,2,2)}$ measures the energy independent ratio between inter- and intravalley scattering. This parameter will be used throughout the following discussion.

TABLE I: The descriptions of the effective relaxation times, based on their scattering processes and origins. 0, x, y, z indicate the impurity potential that give the relaxation times. 0 for the scalar scattering, x, y, z are for the three components of the magnetic scattering.

Description	Spin up (down)	Spin down (up)
	at $K(-K)$	at $K(-K)$
Intravalley (0, z)	$\tau_{(1,1,1)}$	$\tau_{(2,1,1)}$
Intravalley (x, y)	$\tau_{(1,2,1)}$	$\tau_{(2,2,1)}$
Intervalley (0, z)	$\tau_{(1,1,2)}$	$\tau_{(2,1,2)}$
Intervalley (x, y)	$\tau_{(1,2,2)}$	$\tau_{(2,2,2)}$
Skew scattering	$\tau_{(1,1,3)}$	$\tau_{(2,1,3)}$

C. Vertex correction to Velocity

One of the direct and important disorder effects on the SHC is due to the vertex correction to velocity.³⁰ A

well-known example is for the Rashba model where the vertex correction cancels exactly the intrinsic SHC.^{18–20} In contrast, the spin-valley coupled model with a large band gap considered here gives qualitatively different vertex correction to velocity. This is also different from the discussion on the single-flavor massive Dirac fermions;²⁷ here the extra valley degree of freedom and intervalley scattering also modify the vertex correction.

The diagram for the corrected velocity vertex \tilde{v}_y is shown in Fig. 4 (a). Since the low-energy effective model requires that $k \ll |\mathbf{K} - (-\mathbf{K})|$, the valley index should be conserved.²⁹ This means only diagonal terms $\tilde{v}_y^K, \tilde{v}_y^{-K}$ (short for $\tilde{v}_y^{KK}, \tilde{v}_y^{-K-K}$) are possible. Depending on the doping level, one or multiple bands can cross the Fermi level and give different forms of vertex correction.

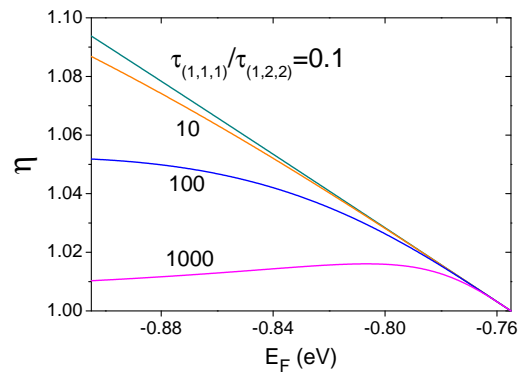


FIG. 2: The factor η that corrects the velocity in the lightly hole-doped regime as functions of Fermi energy E_F for different $\tau_{(1,1,1)}/\tau_{(1,2,2)}$, the ratio of intravalley scattering time to intervalley scattering time. All parameters are adopted for MoS₂ from Ref. [4].

Single-band case: In this case, the Fermi level is located in spin-orbit split gap at the valence band top, as shown in Fig. 1. According to the ladder diagram expansion in Fig. 4 (a), a self-consistent equation can be constructed

$$\begin{pmatrix} \tilde{v}_{y\mathbf{k}}^K \\ \tilde{v}_{y\mathbf{k}}^{-K} \end{pmatrix} = \begin{pmatrix} v_{y\mathbf{k}}^K \\ v_{y\mathbf{k}}^{-K} \end{pmatrix} + \sum_{\mathbf{k}'} \begin{pmatrix} f(K, K) & f(K, -K) \\ f(-K, K) & f(-K, -K) \end{pmatrix} \times \begin{pmatrix} \tilde{v}_{y\mathbf{k}'}^K \\ \tilde{v}_{y\mathbf{k}'}^{-K} \end{pmatrix}, \quad (14)$$

with the kernel function f defined as

$$f(\alpha, \beta) = \langle U_{\mathbf{k}\mathbf{k}'}^{\alpha\beta} U_{\mathbf{k}'\mathbf{k}}^{\beta\alpha} \rangle_{dis} G_{\mathbf{k}',\beta}^R G_{\mathbf{k},\beta}^A. \quad (15)$$

Due to the particular form of the intervalley scattering in Eq. (9), the correlation $\langle U_{\mathbf{k}\mathbf{k}'}^{\alpha\beta} U_{\mathbf{k}'\mathbf{k}}^{\beta\alpha} \rangle_{dis}$ as well as $f(\alpha, \beta)$ for $\alpha \neq \beta$ become angle independent, implying that the matrix in Eq. (14) is decoupled. We can assume the form of the corrected velocity $\tilde{v}_{y\mathbf{k}}^\alpha = \eta v_{y\mathbf{k}}^\alpha$ ($\alpha = K, -K$) and obtain that

$$\eta = \frac{1}{1 - w_1^2 \chi_1^2 (\tau/\tau_{(1,1,1)})}. \quad (16)$$

We can see that the intervalley scattering enters η only through τ , which is defined in Eq. (10). η gets suppressed ($\rightarrow 1$) by the intervalley scattering as $1/\tau_{(1,2,2)} \gg 1/\tau_{(1,1,1)}$. The same calculation applies to the spin current operator j_x^z , and we have the corrected $\tilde{j}_x^z = \eta j_x^z$ at each valley. Numerical results are shown in Fig. 2, where η increases from 1 as the Fermi energy moves away from the valence band edge. Different from usual multi-band systems, the correction here does not modify the intrinsic SHC directly, and the reason is due to the conservation of valley index mentioned above. Later we will show that the correction is manifested through the extrinsic spin Hall effect.

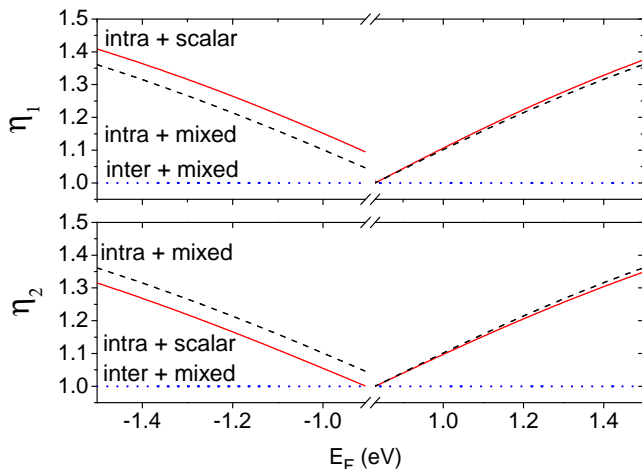


FIG. 3: Vertex correction factors η_1 and η_2 as functions of the Fermi energy E_F , in the presence of the scalar potential induced intravalley scattering (solid), intravalley scattering with the equal contribution from the scalar and magnetic potentials (dashed), and intervalley scattering with the equal scalar and magnetic contributions (dotted). All bands in both K and $-K$ valleys are included. The positive and negative E_F correspond to electron- and hole-doped regimes, respectively. All parameters are adopted for MoS_2 from Ref. [4].

Multi-band case: We now consider the multiband effect on vertex correction when the system becomes electron- or heavily hole-doped. The forms of relaxation times in this case are shown in Appendix A. We assume that $\tilde{v}_{y\mathbf{k}}^n = \eta_n v_{y\mathbf{k}}^n$ ($n = 1, 2$ for $\tau_s = \pm 1$). It can be demonstrated that

$$\begin{pmatrix} \eta_1 \\ \eta_2 \end{pmatrix} = \begin{pmatrix} 1 \\ 1 \end{pmatrix} + \begin{pmatrix} \tau_{K,\uparrow}/\tau_{(1,1,1)} & \tau_{K,\downarrow}/\tau_{(2,2,1)} \\ \tau_{K,\uparrow}/\tau_{(1,2,1)} & \tau_{K,\downarrow}/\tau_{(2,1,1)} \end{pmatrix} \times \begin{pmatrix} \chi_1^2 w_1^2 \eta_1 \\ \chi_2^2 w_2^2 \eta_2 \end{pmatrix}. \quad (17)$$

After solving these equations, $\eta_{1,2}$ can be derived. The same argument can be applied to the spin current operator $\tilde{j}_{x\mathbf{k}}^z = \eta_n j_{x\mathbf{k}}^z$. The numerical results for η_1 and η_2 are given in Fig. 3, and three different cases are compared: pure intravalley scalar scattering, pure intravalley

(intervalley) scattering with equal scalar and magnetic contributions. For the intravalley scattering, η_1 and η_2 increase as the Fermi energy moves away from the band edges, much like in the lightly hole-doped regime. In contrast, there is no correction ($\eta_{1,2} = 1$) for the pure intervalley scattering due to the loss of coherence.

IV. SPIN HALL CONDUCTIVITY OF THE VALENCE BAND AT VALLEY K

The SHC σ_{xy}^z is the response function of spin current

$$j_x^z = \frac{\hbar}{4} \{v_x, \sigma_z \otimes I\} \quad (18)$$

to the charge current j_y . Note that in spin-orbit coupled systems, the spin in general is not a conserved quantity.³¹ However, in MX_2 monolayers, because of the in-plane mirror symmetry, the z -component of the spin is conserved and the above definition is valid. Similar to the anomalous Hall effect,^{27,32,33} the spin Hall effect has both intrinsic and extrinsic contributions. The SHC can be derived from the Kubo-Streda formula.^{34,35} In the weak scattering limit, the conductivity is separated into $\sigma_{xy}^z = \sigma_{xy}^{z,I} + \sigma_{xy}^{z,II}$, where $\sigma_{xy}^{z,I}$, $\sigma_{xy}^{z,II}$ are the contribution near the Fermi surface and intrinsic contribution from the Fermi sea, respectively. The intrinsic SHC is independent of disorder, but determined by the Berry curvature of occupied states (the Fermi sea contribution).^{6,36} On the other hand, the extrinsic SHC is given by the disorder-dependent part of $\sigma_{xy}^{z,I}$ term

$$\sigma_{xy}^{z,I} = \frac{e\hbar}{2\pi S} \text{Tr} \langle j_x^z G^R(E_F) v_y G^A(E_F) \rangle, \quad (19)$$

where $G^{R/A}$ is the retarded (advanced) Green's function dressed by the impurity scattering. e is the electron charge. For convenience, we will multiply a factor $2e/\hbar$ to the SHC, so that it has the units of the charge conductivity. In this section, we focus on the lightly hole-doped regime as shown in Fig. 1, when the Fermi energy intersects just a single band at each valley.

A. Intrinsic spin Hall conductivity

In monolayer MX_2 , the z -component of the spin is conserved in each band, so the derivation of the SHC is equivalent to two copies of the anomalous Hall conductivity. The intrinsic anomalous Hall effect originates from the Berry curvature⁶

$$\Omega_n^z(\mathbf{k}) = \hat{z} \cdot \nabla_{\mathbf{k}} \times \langle u_n(\mathbf{k}) | i \nabla_{\mathbf{k}} | u_n(\mathbf{k}) \rangle \quad (20)$$

of occupied states, where $u_n(\mathbf{k})$ is the eigenfunction for band n and wave vector \mathbf{k} , and \hat{z} the unit vector along the z axis. Time-reversal symmetry requires that $\Omega_n(-\mathbf{k}) = -\Omega_n(\mathbf{k})$, leading to opposite anomalous Hall

conductivity for different valleys. When combined with the spin-valley coupled property, each valley gives the same contribution to the SHC. The intrinsic spin Hall effect has been studied by first-principles calculations for this system.¹⁷

At zero temperature, the intrinsic SHC is given by

$$\sigma_{xy}^{int} = \frac{e^2}{h} \sum_{n=1,2} (-1)^n \int \frac{d^2\mathbf{k}}{(2\pi)^2} \Omega_n^z(\mathbf{k}) \Theta(E_F - E_{\mathbf{k}}), \quad (21)$$

where at valley K , $n = 1, 2$ corresponds to spin up and down, respectively. Based on the low-energy effective model, the intrinsic SHC is found as

$$\sigma_{xy}^{int} = \frac{e^2}{2h} (1 - \cos \theta_1), \quad (22)$$

where θ_1 is defined by Eq. (5) on the Fermi surface. Obviously, σ_{xy}^{int} reaches its maximum at the band edge of the second highest valence band.

B. Extrinsic spin Hall conductivity

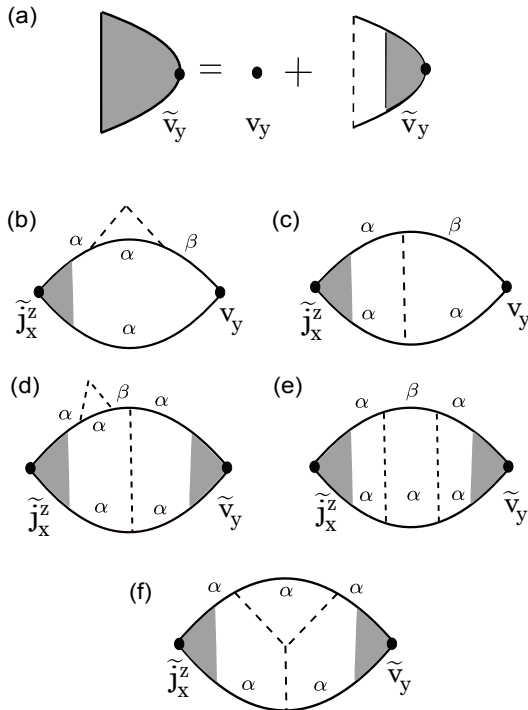


FIG. 4: (a) Ladder-diagram correction to velocity vertex shown in grey region. (b)-(f) Diagrams contributing to the extrinsic spin Hall conductivity. α and β denote different bands and dashed lines refer to correlated disorder scattering.

The extrinsic spin Hall effect comes from electrons near the Fermi surface when they are scattered by impurities and disorders, and can be divided into from side-jump²⁵ and skew-scattering mechanisms.²⁴ The Feynman

diagrams to calculate them are depicted in Fig. 4 (b)-(f).^{27,32,37} In the semiclassical picture, side-jump terms can be further classified into three contributions. (1) From the anomalous distribution function in Fig. 4 (b) and (c); (2) From the coordinate shift by making a 180° rotation of Fig. 4 (b) and (c) followed by exchanging symbols j_x^z and v_y ; (3) skew scattering-induced side jump in Fig. 4 (d) and (e). The third-order correlation-related skew scattering is drawn in Fig. 4 (f). For each diagram in Fig. 4 (b)-(f), there exists a symmetric copy by exchanging α and β .^{27,32} Here α and β denotes different combinations of indices including valley, spin, and band.

Diagrams in Fig. 4 (b)-(e) all contain at least one asymmetric correlation function $\langle U^{\alpha\alpha} U^{\alpha\beta} \rangle_{dis}$, which is angle-dependent and may lead to nonvanishing results. However, for the valley index, the correlations $\langle U^{KK} U^{K-K} \rangle_{dis}, \langle U^{-K-K} U^{-KK} \rangle_{dis}$ are forbidden due to the violation of the valley conservation. This means that different valleys are decoupled in the side-jump mechanism and can be treated separately.

Back to the spin index, the correlation functions $\langle U^{\uparrow\uparrow} U^{\uparrow\downarrow} \rangle_{dis}, \langle U^{\downarrow\downarrow} U^{\downarrow\uparrow} \rangle_{dis}$ are neglected since the scattering in different directions is assumed to be uncorrelated. This implies that we can further decouple the spin part in the side-jump mechanism even when the scattering is spin-dependent. Hence we can limit α and β to only band index. This is supported by the fact that the interband scattering can contribute to the spin Hall effect via virtual interband transitions. Now the calculation becomes similar to that for the anomalous Hall effect,²⁷ and side-jump Hall conductivity at each valley has the form

$$\sigma_{xy}^{sj} = -\frac{e^2}{2h} \eta \sin^2 \theta_1 \cos \theta_1 \frac{\tau}{\tau_{(1,1,1)}} \times \left(1 + \frac{3}{16} \eta \sin^2 \theta_1 \frac{\tau}{\tau_{(1,1,1)}} \right), \quad (23)$$

while the skew-scattering Hall conductivity reads

$$\sigma_{xy}^{sk} = \frac{e^2}{8h} \eta^2 \sin^4 \theta_1 \cos \theta_1 \left(\frac{\tau}{\tau_{(1,1,3)}} \right)^2. \quad (24)$$

It is clear that σ_{xy}^{sj} has opposite sign compared with σ_{xy}^{int} , while σ_{xy}^{sk} shows the same sign, which means that the skew scattering enhances the intrinsic spin-Hall effect while the side jump suppresses it. Note that σ_{xy}^{int} and σ_{xy}^{sj} are independent of the total disorder concentration, while $\sigma_{xy}^{sk} \sim n^{-1}$. This implies that in the clean limit the skew scattering becomes dominant. On the other hand, the scalar and magnetic scattering do not make much difference since the spin part is decoupled in the side-jump mechanism. The only difference is that magnetic scattering can contribute to the intervalley scattering, and thus modify the total scattering time.

C. Total contribution

The total SHC in the lightly hole-doped monolayer MX_2 reads

$$\sigma_{xy}^z = 2 \times (\sigma_{xy}^{int} + \sigma_{xy}^{sj} + \sigma_{xy}^{sk}), \quad (25)$$

where the factor 2 comes from the valley degeneracy. At a low doping level when $|E_F| \ll \Delta$, σ_{xy}^{int} and σ_{xy}^{sj} are of the order of $O(\Delta^{-2})$, while σ_{xy}^{sk} is of the order of $O(\Delta^{-4}, n^{-1})$. This means that σ_{xy}^{sk} only dominates in the ultraclean limit, otherwise this term can be safely neglected. The results for the intrinsic and side-jump contributions are shown in Fig. 5. It is clear that these two terms always have opposite signs. Both the intrinsic (σ_{xy}^{int}) and side-jump (σ_{xy}^{sj}) contributions depend on the Fermi energy [Figs. 5 (a) and 5 (b)], while the side-jump contribution also depends on the ratio [Fig. 5 (b)]

$$\frac{\tau_{(1,1,1)}}{\tau_{(1,2,2)}} = \frac{n_m t_x^2 + n_m t_y^2}{n_0 u_0^2 + n_m u_z^2}, \quad (26)$$

which measures the energy-independent scattering ratio between the inter- and intravalley scattering. σ_{xy}^{sj} can be suppressed by the intervalley scattering. As a result, by tuning $\tau_{(1,1,1)}/\tau_{(1,2,2)}$, the total SHC, as a summation of the intrinsic and side-jump contributions, could change sign. This may offer a new way to estimate the strength of the intervalley scattering in MX_2 monolayers.

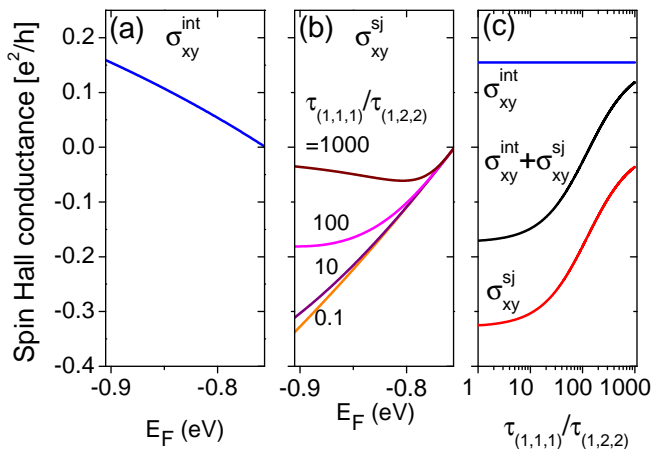


FIG. 5: The spin Hall conductivity in the lightly hole-doped regime. (a) The intrinsic spin Hall conductivity as a function of the Fermi energy E_F . (b) The side-jump spin Hall conductivity vs E_F for different $\tau_{(1,1,1)}/\tau_{(1,2,2)}$, the ratio of the intervalley scattering to intravalley scattering. (c) The intrinsic and side-jump spin Hall conductivities as functions of $\tau_{(1,1,1)}/\tau_{(1,2,2)}$ at $E_F = -0.90eV$. All parameters are adopted for MoS_2 from Ref. [4].

V. MULTI-BAND SPIN HALL CONDUCTIVITY

In this section we extend the above discussion to the multiband case, where at each valley, two bands contribute to the SHC. This situation corresponds to the electron- or heavily hole-doped cases. The vertex correction in this regime has been discussed in Sec. III.

A. Intrinsic spin Hall conductivity

In the electron-doped regime, the intrinsic SHC reads

$$\sigma_{xy}^{int} = \frac{e^2}{2h} (\cos \theta_1 - \cos \theta_2), \quad (27)$$

where $\theta_{1,2}$ are defined in Eq. (5) on the Fermi surface. When tuned to the heavily hole-doped regime, the SHC becomes

$$\sigma_{xy}^{int} = -\frac{e^2}{2h} (\cos \theta_1 - \cos \theta_2). \quad (28)$$

B. Extrinsic spin Hall conductivity

In the diagrammatic language, the side-jump contribution σ_{xy}^{sj} comes from the asymmetric scattering correlation. However, in the present case the two bands at each valley have opposite spin-polarization and thus the asymmetric correlation between them must vanish. As a result, σ_{xy}^{sj} is contributed independently by each band, which reads

$$\begin{aligned} \sigma_{xy}^{sj} = & -\frac{e^2}{2h} \left[\eta_1 \sin^2 \theta_1 \cos \theta_1 \frac{\tau_{\uparrow,K}}{\tau_{(1,1,1)}} \right. \\ & \times \left(1 + \frac{3\eta_1}{16} \sin^2 \theta_1 \frac{\tau_{\uparrow,K}}{\tau_{(1,1,1)}} \right) \\ & - \eta_2 \sin^2 \theta_2 \cos \theta_2 \frac{\tau_{\downarrow,K}}{\tau_{(2,1,1)}} \\ & \left. \times \left(1 + \frac{3\eta_2}{16} \sin^2 \theta_2 \frac{\tau_{\downarrow,K}}{\tau_{(2,1,1)}} \right) \right], \end{aligned} \quad (29)$$

for both electron and heavily hole-doped regime. Since there are more channels now, the relaxation times become band-dependent and the expressions can be found in Appendix A. In general, time-reversal symmetry requires that $\tau_{\uparrow,-K} = \tau_{\downarrow,K}$ and $\tau_{\downarrow,-K} = \tau_{\uparrow,K}$.

As for the skew scattering, the argument is essentially the same and we have

$$\begin{aligned} \sigma_{xy}^{sk} = & \mp \frac{e^2}{8h} \left[\eta_1^2 \sin^4 \theta_1 \cos \theta_1 \left(\frac{\tau_{\uparrow,K}}{\tau_{(1,1,3)}} \right)^2 \right. \\ & \left. - \eta_2^2 \sin^4 \theta_2 \cos \theta_2 \left(\frac{\tau_{\downarrow,K}}{\tau_{(2,1,3)}} \right)^2 \right], \end{aligned} \quad (30)$$

where \mp refers to electron- and heavily hole-doped regime, respectively.

C. Total contribution

The total contribution is given by the summation of σ_{xy}^{int} and σ_{xy}^{sj} ; σ_{xy}^{sk} is neglected. Three different cases are compared in Fig. 6: pure intravalley scalar scattering, pure intravalley (intervalley) scattering with equal scalar and magnetic contributions. Obviously, the SHC has a much larger value in hole-doped regime than in electron-doped regime, due to the existence of large spin splitting in the valence band. Similar to the conclusion in the last section, by tuning the ratio of intra- to intervalley scattering time, i.e. $\tau_{(1,1,1)}/\tau_{(1,1,2)}$, the SHC exhibits a sign change in the hole-doped regime in Fig. 7 (a), while this is not the case for the electron-doped regime. Moreover, different from the single-band case where the intervalley and magnetic scattering are locked, here the intervalley and magnetic scattering can be tuned independently. As a result, it is found that by tuning the ratio of the scalar to magnetic scattering time, i.e., $n_x u_x^2/n_0 u_0^2$, the SHC again exhibits a sign change in the hole-doped regime, as shown in Fig. 7 (b).

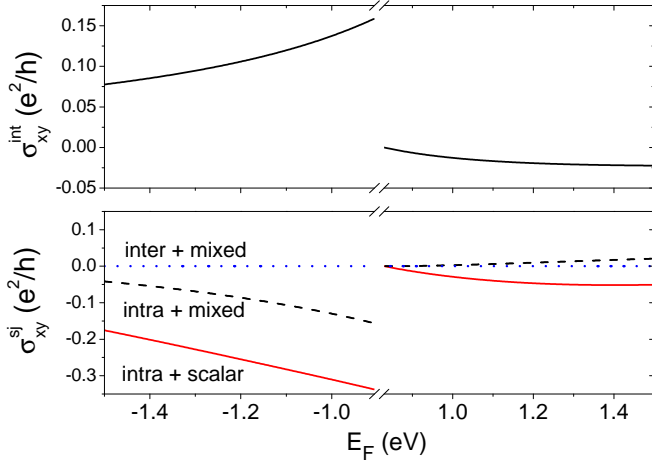


FIG. 6: The intrinsic (σ_{xy}^{int}) and side-jump (σ_{xy}^{sj}) spin Hall conductivity in the electron- and heavily hole-doped regime as functions of the Fermi energy E_F . Solid, dashed, and dotted lines correspond to the cases with the scalar potential induced intravalley scattering, intravalley scattering with the equal contribution from the scalar and magnetic potentials, and intervalley scattering with the equal scalar and magnetic contributions, respectively. All parameters are adopted for MoS₂ from Ref. [4].

VI. DISCUSSION AND CONCLUSION

As discussed in Secs. IV and V, the side-jump and intrinsic contributions are comparable with each other, highlighting the important role of disorder in the spin Hall effect in monolayer MX_2 . Consider a hole-doped MoS₂ sample with a carrier density of $n_h = 1.0 \times 10^{13} \text{cm}^{-2}$, for which the Fermi energy lies in the spin-

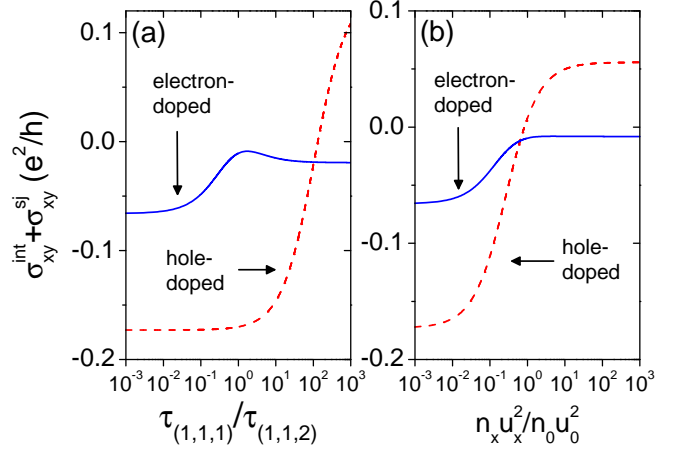


FIG. 7: The total spin Hall conductivity $\sigma_{xy}^{int} + \sigma_{xy}^{sj}$ as a function of (a) ratio of intra- to intervalley scattering time and (b) ratio of scalar to magnetic scattering. $E_F = 1.2$ eV for electron-doped case (solid), and $E_F = -1.0$ eV for hole-doped case (dashed). In (a), the magnetic scattering is absent, and in (b) the intervalley scattering is absent. All parameters are adopted for MoS₂ from Ref. [4].

split valence bands. In the absence of the intervalley scattering, the intrinsic and side-jump contributions are $\sigma_{int} = 0.90 \times 10^{-2} e^2/\hbar$ and $\sigma_{sj} = -1.83 \times 10^{-2} e^2/\hbar$, respectively. As a result, the total SHC becomes $\sigma_{xy}^z = -0.93 \times 10^{-2} e^2/\hbar$, which is comparable with those in semiconductors GaAs, Ge and AlAs.^{38,39} Experimentally, the SHC can be evaluated by fitting the measured spin accumulation at edges.

Although our calculations are mainly based on the low-energy effective model at $\pm K$, the conclusion is valid even when the Γ valley^{40–42} is involved. The reason is that the existence of the large effective mass and small spin splitting at Γ valley results in a negligible spin-Hall conductivity.

In summary, we have studied the spin Hall conductivity of monolayer MoS₂ with both intrinsic and extrinsic contributions. We find that in this large-gap system the side-jump contribution is comparable with the intrinsic contribution. The side-jump and intrinsic contributions have opposite signs. The side-jump contribution can be suppressed by the intervalley scattering. By tuning the ratio of intra- to intervalley scattering, the total spin Hall conductivity shows a sign change in hole-doped samples, which can be used to measure the strength of the intervalley scattering.

We acknowledge useful discussion with Dimitrie Culcer. This work was supported by the U.S. Department of Energy, Office of Basic Energy Sciences, Materials Sciences and Engineering Division (W.S.) and by AFOSR Grant No. FA9550-12-1-0479 (D.X.)

Appendix A: Relaxation time

We define a set of relaxation times

$$\frac{1}{\tau_{(n,1,1)}} = \frac{2\pi}{\hbar} N_n (n_0 u_0^2 + n_z u_z^2), \quad (\text{A1})$$

$$\frac{1}{\tau_{(n,2,1)}} = \frac{2\pi}{\hbar} N_n (n_x u_x^2 + n_y u_y^2), \quad (\text{A2})$$

$$\frac{1}{\tau_{(n,1,2)}} = \frac{2\pi}{\hbar} N_n (n_0 t_0^2 + n_z t_z^2), \quad (\text{A3})$$

$$\frac{1}{\tau_{(n,2,2)}} = \frac{2\pi}{\hbar} N_n (n_x t_x^2 + n_y t_y^2), \quad n = 1, 2 \quad (\text{A4})$$

which are functions of scattering potential, disorder concentration and density of states. Then the relaxation time in multiband cases can be conveniently expressed by using these new definitions. For example, in the electron-doped regime at valley K the relaxation time reads

$$\begin{aligned} \frac{1}{\tau_{\uparrow,K}} &= \frac{1}{\tau_{(1,1,1)}} (\chi_1^4 + w_1^4) + \frac{1}{\tau_{(2,2,1)}} (\chi_1^2 \chi_2^2 + w_1^2 w_2^2) \\ &+ \frac{1}{\tau_{(2,1,2)}} \chi_1^2 \chi_2^2 + \frac{1}{\tau_{(1,2,2)}} \chi_1^4, \end{aligned} \quad (\text{A5})$$

$$\begin{aligned} \frac{1}{\tau_{\downarrow,K}} &= \frac{1}{\tau_{(2,1,1)}} (\chi_2^4 + w_2^4) + \frac{1}{\tau_{(1,2,1)}} (\chi_1^2 \chi_2^2 + w_1^2 w_2^2) \\ &+ \frac{1}{\tau_{(1,1,2)}} \chi_1^2 \chi_2^2 + \frac{1}{\tau_{(2,2,2)}} \chi_2^4. \end{aligned} \quad (\text{A6})$$

And time-reversal symmetry guarantees that $\tau_{\uparrow,-K} = \tau_{\downarrow,K}$ and $\tau_{\downarrow,-K} = \tau_{\uparrow,K}$. Similarly in the heavily hole-doped regime we have

$$\begin{aligned} \frac{1}{\tau_{\uparrow,K}} = \frac{1}{\tau_{\downarrow,-K}} &= \frac{1}{\tau_{(1,1,1)}} (\chi_1^4 + w_1^4) + \frac{1}{\tau_{(2,1,2)}} w_1^2 w_2^2 \\ &+ \frac{1}{\tau_{(2,2,1)}} (\chi_1^2 \chi_2^2 + w_1^2 w_2^2) + \frac{1}{\tau_{(1,2,2)}} w_1^4, \end{aligned} \quad (\text{A7})$$

$$\begin{aligned} \frac{1}{\tau_{\downarrow,K}} = \frac{1}{\tau_{\uparrow,-K}} &= \frac{1}{\tau_{(2,1,1)}} (\chi_2^4 + w_2^4) + \frac{1}{\tau_{(1,1,2)}} w_1^2 w_2^2 \\ &+ \frac{1}{\tau_{(1,2,1)}} (\chi_1^2 \chi_2^2 + w_1^2 w_2^2) + \frac{1}{\tau_{(2,2,2)}} w_2^4. \end{aligned} \quad (\text{A8})$$

Also, the relaxation times for the skew scattering can be given as³²

$$\frac{1}{\tau_{(1,1,3)}^2} = \frac{4\pi^3 a^2 t^2}{\hbar^2} N_1^3 (n_0 v_0^3 + n_z v_z^3), \quad (\text{A9})$$

$$\frac{1}{\tau_{(2,1,3)}^2} = \frac{4\pi^3 a^2 t^2}{\hbar^2} N_2^3 (n_0 v_0^3 + n_z v_z^3), \quad (\text{A10})$$

and it is clear that $1/\tau_{(1,1,3)}^2$ and $1/\tau_{(2,1,3)}^2$ are proportional to disorder concentration n_{dis} .

-
- ¹ Q. H. Wang, K. Kalantar-Zadeh, A. Kis, J. N. Coleman, and M. S. Strano, *Nature Nanotech.* **7**, 699 (2012), and references therein.
- ² A. Splendiani, L. Sun, Y. Zhang, T. Li, J. Kim, C.-Y. Chim, G. Galli, and F. Wang, *Nano Lett.* **10**, 1271 (2010).
- ³ K. F. Mak, C. Lee, J. Hone, J. Shan and T. F. Heinz, *Phys. Rev. Lett.* **105**, 136805 (2010).
- ⁴ D. Xiao, G.-B. Liu, W. Feng, X. Xu, and Wang Yao, *Phys. Rev. Lett.* **108**, 196802 (2012).
- ⁵ T. Cao, G. Wang, W. Han, H. Ye, C. Zhu, J. Shi, Q. Niu, P. Tan, E. Wang, B. Liu, and J. Feng, *Nat. Commun.* **3**, 887 (2012).
- ⁶ D. Xiao, M.-C. Chang, and Q. Niu, *Rev. Mod. Phys.* **82**, 1959 (2010).
- ⁷ D. Xiao, W. Yao, and Q. Niu, *Phys. Rev. Lett.* **99**, 236809 (2007).
- ⁸ W. Yao, D. Xiao, and Q. Niu, *Phys. Rev. B* **77**, 235406 (2008).
- ⁹ H. Zeng, J. Dai, W. Yao, D. Xiao, and X. Cui, *Nat. Nanotech.* **7**, 490 (2012).
- ¹⁰ K. F. Mak, K. He, J. Shan, and T. F. Heinz, *Nat. Nanotech.* **7**, 494 (2012).
- ¹¹ S. Wu, J. S. Ross, G.-B. Liu, G. Aivazian, A. Jones, Z. Fei, W. Zhu, D. Xiao, W. Yao, D. Cobden, and X. Xu, *Nat. Phys.* **9**, 149 (2013).
- ¹² Z. Y. Zhu, Y. C. Cheng, and U. Schwingenschlogl, *Phys. Rev. B* **84**, 153402 (2011).
- ¹³ H. Ochoa, and R. Roldan, arXiv:1303.5860 (2013).
- ¹⁴ H.-Z. Lu, W. Yao, D. Xiao, S.-Q. Shen, *Phys. Rev. Lett.* **110**, 016806 (2013).
- ¹⁵ S. Murakami, N. Nagaosa, and S. C. Zhang, *Science* **301**, 1348 (2003).
- ¹⁶ J. Sinova, D. Culcer, Q. Niu, N. A. Sinitsyn, T. Jungwirth, A. H. MacDonald, *Phys. Rev. Lett.* **92**, 126603 (2004).
- ¹⁷ W. Feng, Y. Yao, W. Zhu, J. Zhou, W. Yao, and D. Xiao, *Phys. Rev. B* **86**, 165108 (2012).
- ¹⁸ J.-I. Inoue, G. E. W. Bauer, and L. W. Molenkamp, *Phys. Rev. B* **70**, 041303 (2004).
- ¹⁹ R. Raimondi, and P. Schwab, *Phys. Rev. B* **71**, 033311 (2005).
- ²⁰ E. I. Rashba, *Phys. Rev. B* **70**, 201309 (2004).
- ²¹ M. I. Dyakonov, and V. I. Perel, *JETP Lett.* **13**, 467 (1971).
- ²² M. I. Dyakonov, and V. I. Perel, *Phys. Lett. A* **35**, 459 (1971).
- ²³ J. E. Hirsch, *Phys. Rev. Lett.* **83**, 1834 (1999).
- ²⁴ J. Smit, *Physica (Amsterdam)* **21**, 877 (1955).
- ²⁵ L. Berger, *Phys. Rev. B* **2**, 4559 (1970).
- ²⁶ X. Z. Yan and C. S. Ting, *Phys. Rev. Lett.* **101**, 126801 (2008).
- ²⁷ N. A. Sinitsyn, A. H. MacDonald, T. Jungwirth, V. K. Dugaev, and J. Sinova, *Phys. Rev. B* **75**, 045315 (2007).
- ²⁸ W.-K. Tse, and S. D. Sarma, *Phys. Rev. Lett.* **96**, 056601 (2006).
- ²⁹ H. Suzuura, and T. Ando, *Phys. Rev. Lett.* **89**, 266603 (2002).

- ³⁰ N. H. Shon and T. Ando, *J. Phys. Soc. Jpn.* **67**, 2421 (1998).
- ³¹ J. Shi, P. Zhang, D. Xiao, and Q. Niu, *Phys. Rev. Lett.* **96**, 076604 (2006).
- ³² S. A. Yang, H. Pan, Y. Yao, and Q. Niu, *Phys. Rev. B* **83**, 125122 (2011).
- ³³ N. Nagaosa, J. Sinova, S. Onoda, A. H. MacDonald, and N. P. Ong, *Rev. Mod. Phys.* **82**, 1539 (2010).
- ³⁴ A. Crepieux and P. Bruno, *Phys. Rev. B* **64**, 014416 (2001).
- ³⁵ P. Streda, *J. Phys. C* **15**, L717 (1982).
- ³⁶ G. Sundaram and Q. Niu, *Phys. Rev. B* **59**, 14915 (1999).
- ³⁷ H.-Z. Lu, and S.-Q. Shen, arXiv:1302.6688 (2013).
- ³⁸ Y. G. Yao, and Z. Fang, *Phys. Rev. Lett.* **95**, 156601 (2005).
- ³⁹ G. Y. Guo, Y. G. Yao, and Q. Niu, *Phys. Rev. Lett.* **94**, 226601 (2005).
- ⁴⁰ T. Cheiwchanchamnangij and W. R. L. Lambrecht, *Phys. Rev. B* **85**, 205302 (2012).
- ⁴¹ H. Shi, H. Pan, Y.-W. Zhang, and B. I. Yakobson, *Phys. Rev. B* **87**, 155304 (2013).
- ⁴² J. K. Ellis, M. J. Lucero, and G. E. Scuseria, *Appl. Phys. Lett.* **99**, 261908 (2011).